Rotational transitions of C3N– induced by collision with H2

Miguel Lara-Moreno, Thierry Stoecklin, Philippe Halvick

MNRAS **000**, 1–8 (2015) Preprint 6 March 2019 Compiled using MNRAS LATEX style file v3.0

Rotational transitions of C_3N^- induced by collision with H_2

Miguel Lara-Moreno,[1] Thierry Stoecklin,[1]⋆ Philippe Halvick[1]
[1] *Université de Bordeaux, ISM, UMR 5255, 33405, Talence, France*

6 March 2019

ABSTRACT

Rate coefficients for state-to-state rotational transitions of C_3N^- induced by collision with both *ortho*– and *para*–H_2 are presented. Quantum calculations are performed at the close-coupling level using the uniform J-shifting method and a new potential energy surface specially developed for this purpose. Rate coefficients are obtained for state-to-state transitions among the first 28 rotational levels of C_3N^- and for temperatures ranging from 10 to 300 K. The *para*–H_2 rate coefficients are shown to differ strongly from the mass-scaled He rate coefficients previously computed. The *ortho*– and *para*–H_2 rate coefficients are very similar, as it was already observed for the rotational transitions of CN^- and C_6H^-. There is also an unexpected similarity between the rates coefficients of the rotational de-excitations of CN^-, C_3N^-, and C_6H^-. This may open to door to quantitative extrapolations of the rate coefficients for larger anions.

Key words: keyword1 – keyword2 – keyword3

1 INTRODUCTION

Although the existence and possible detection of anions in the interstellar medium (ISM) was proposed long ago (Dalgarno & McCray 1973; Sarre 1980; Herbst 1981), it was not till last decade that the first molecular anion C_6H^- was detected in the circumstellar envelope IRC+10216 and in the dense molecular cloud TMC-1 (McCarthy et al. 2006). So far, only six anion (CN^-, C_3N^-, C_5N^-, C_4H^-, C_6H^-, C_8H^-) have been detected in carbon rich interstellar sources (Brünken et al. 2007; Cernicharo et al. 2007, 2008; Thaddeus et al. 2008; Agúndez et al. 2010). The abundances of these molecules could in principle be extracted from the spectroscopic observations through radiative transfer calculations. This procedure however requires the knowledge of rotational state-to-state radiative and collisional rates with H_2 since the latter is by far the most abundant interstellar molecule. Such data are unfortunately scarce especially for the recently detected anions. Up to now, the only available data are limited to the collisions of H_2 with the CN^- (Kłos & Lique 2011) and C_6H^- (Walker et al. 2017) anions. The rotational excitation rates available involving collisions with C_3N^- are limited to those we recently determined for the collisions with He (Lara-Moreno et al. 2017). Collisional rates with He are often used to estimate those for *para*–H_2 using a scaling law based on the ratio of the reduced masses. The applicability of this approximation is unfortunately unpredictable since it may work well as for example for CS (Denis-Alpizar et al. 2013) while it fails reproducing known collisional rates with *para*–H_2 for a few systems (Lique et al. 2008; Guillon & Stoecklin 2012; Walker et al. 2014).

In the present study we then focus on the calculation of the rotational relaxation rates of C_3N^- in collisions with both *ortho*– and *para*–H_2. We calculate state-to-state transitions among the first 28 rotational levels of C_3N^- for temperatures ranging from 10 to 300 K. While the close coupling (CC) method offers the highest level of accuracy for the calculation of the collisional rates, its application to the H_2 + C_3N^- collision is quite challenging owing to the very small value of the rotational constant of C_3N^-, the large reduced mass of the collisional system and the strong long-range anisotropic potential energy. Similar numerical difficulties were already met in the previous study dedicated to the collisions of C_3N^- with He (Lara-Moreno et al. 2017) and overcome by using the Uniform J-shifting (UJS) method (Zhang & Zhang 1999). It was shown in this previous study that the UJS method gives a very good level of accuracy (less than 5% relative error) while offering large computer time saving. We then use here again the UJS method and compare our results with those obtained previously for the collisions with He. We discuss the possible reason of the failure of the mass scaling approximation for this molecule and evaluate the possibility of using the present rates to predict those for larger anions. The manuscript is organized as follows. A brief account of the potential energy surface (PES) model and the CC method is provided in the following section while the results are discussed in section 3 and the conclusions are presented in section 4.

2 METHODS

2.1 Potential Energy Surface

The PES used in this work was developed using explicitly-correlated coupled-cluster method with single and double excitations and using a perturbative treatment of triple excitations [CCSD(T)-F12] and

⋆ E-mail: thierry.stoecklin@u-bordeaux.fr

the augmented correlation-consistent polarized valence triple-zeta basis set (aug-cc-pVTZ) (Kendall et al. 1992). A brief description of the PES is given below while more details are given in Lara-Moreno et al. (2019). The 4D PES is calculated in body-fixed Jacobi coordinates, namely R the intermolecular distance, θ_1 and θ_2 the rotation angle of H_2 and C_3N^- respectively and ϕ the torsion angle between the two molecules. Since C_3N^- is a long molecule, the interaction energy is strongly anisotropic for small intermonomer separation and a large density of *ab initio* points was then necessary to describe properly this region. A total number of 28339 *ab initio* energies were calculated with R ranging from 2 to 50 a_0, θ_1 from 0° to 90°, θ_2 from 0° to 180°, and ϕ from 0° to 180°. For all these calculations, carried out with the MOLPRO package(Werner et al. 2012), the H_2 bond length was fixed to its vibrationally averaged value in the rovibrational ground state, namely r_{HH} = 1.448736 a_0, while the C_3N^- bond lengths were set to their equilibrium values obtained from CCSD(T)/aug-cc-pV5Z calculations (Kołos et al. 2008), namely $r_{C_1C_2}$ = 2.3653 a_0, $r_{C_2C_3}$ = 2.5817 a_0, and r_{C_3N} = 2.2136 a_0. The basis superposition error was then corrected by means of the counterpoise procedure (Boys & Bernardi 1970) applied to the rigid monomer case.

The functional form of the PES is defined as a linear combination of products of radial functions by angular functions, the latter being a product of associated normalized Legendre polynomials $P_l^m(x)$ and cosine functions:

$$V(R,\theta_1,\theta_2,\phi) = \sum_{\lambda_1\lambda_2\mu} v^{\mu}_{\lambda_1\lambda_2}(R) P^{\mu}_{\lambda_1}(\cos\theta_1) P^{\mu}_{\lambda_2}(\cos\theta_2)\cos\mu\phi \quad (1)$$

with $\lambda_1 \in [0,6]$, $\lambda_2 \in [0,18]$ and $\mu \in [0,4]$. The radial part is defined as the summation of two terms associated with the short-range and long-range contributions:

$$v^{\mu}_{\lambda_1\lambda_2}(R) = w(R) f_{SR}(R) + [1 - w(R)] f_{LR}(R) \quad (2)$$

where the switching function $w(R)$ is an hyperbolic tangent. The short-range contribution $f_{SR}(R)$ was interpolated using a cubic spline method, whereas the long-range part $f_{LR}(R)$ was fitted to reciprocal power functions.

The PES is characterized by large anisotropies and deep potential wells. The global minimum, D_e = 769.75 cm^{-1}, corresponds to a linear geometry where the H_2 molecule faces the C-end of the C_3N^- molecule. A secondary minimum, D_e = 561.77 cm^{-1}, was found for another linear geometry where the H_2 molecule faces the N-end of the C_3N^- molecule. These features are depicted in Figure 1

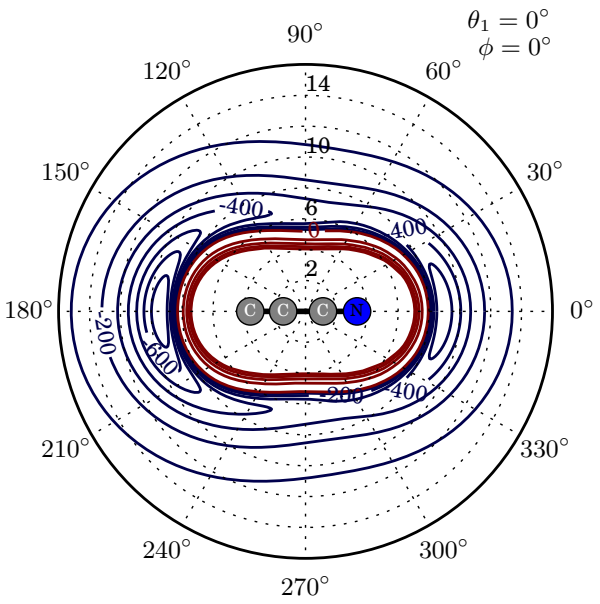

Figure 1. 2D contour plots of the potential energy surface in the (R, θ_2) polar coordinates frame for $\theta_1 = 0°$ and $\phi = 0°$. Contour levels are equally spaced by 100 cm^{-1} and labelled by the energy in cm^{-1}. The contours are blue for negative interaction energy, and red for positive one. The origin of coordinates corresponds to the center of mass of C_3N^-.

2.2 Dynamics

The CC equations for the collision of C_3N^- and H_2 are solved in the space-fixed frame using an improved version of the DIDIMAT code (Guillon et al. 2008) originally developed to study the H_2-HF collision. This code which uses the log-derivative propagator developed by Manolopoulos (1986) was also applied to several other collisional systems like H_2-CO (Chefdeville et al. 2015) or H_2-CS (Denis-Alpizar et al. 2018). By choosing the usual boundary conditions for the radial part of the scattering wave function:

$$\mathbf{G}^J(0) = \mathbf{0}$$

and

$$\mathbf{G}^J(R) \xrightarrow[R\to\infty]{} \mathbf{J}^J(R)\mathbf{A}^J - \mathbf{N}^J(R)\mathbf{B}^J \quad (3)$$

and using the familiar definition of the $\mathbf{K}^J$ and $\mathbf{T}^J$ matrices

$$\mathbf{K}^J = \mathbf{B}^J \left(\mathbf{A}^J\right)^{-1}$$
$$\mathbf{T}^J = -2i\mathbf{K}^J \left(\mathbf{I} - i\mathbf{K}^J\right)^{-1} \quad (4)$$

where $\mathbf{N}^J(R)$ and $\mathbf{J}^J(R)$ are diagonal matrices of spherical Ricatti-Bessel functions of the first and second kinds $\tilde{j}_l$ and $\tilde{n}_l$ while the superscript J accounts for the total angular momentum quantum number. We then calculate the standard state-to-state transition probabilities as a function of the $\mathbf{T}^J$ matrix elements,

$$P^J_{j_1j_2\to j_1'j_2'}(E) = \frac{1}{(2j_1+1)(2j_2+1)} \sum_{j_{12}=|j_1-j2|}^{j_1+j_2} \sum_{j'_{12}=|j_1'-j_2'|}^{j_1'+j_2'} \times \sum_{l=|J-j_{12}|}^{J+j_{12}} \sum_{l'=|J-j_{12}'|}^{J+j_{12}'} T^J_{j_1,j_2,j_{12},l,j_1',j_2',j_{12}',l'}(E) \quad (5)$$

where j_1, j_1', j_2, j_2' denote the initial and final rotational states of H_2 and C_3N^- respectively. Subsequently one obtains the state-to-state inelastic cross sections:

$$\sigma_{j_1j_2\to j_1'j_2'}(E) = \frac{\pi}{k^2_\gamma} \sum_{J=0}^{\infty} (2J+1) P^J_{j_1j_2\to j_1'j_2'}(E) \quad (6)$$

Finally, the state-selected rotational relaxation rates of C_3N^- in collisions with H_2 are obtained by thermally averaging the inelastic cross sections $\sigma_{j_1j_2\to j_1'j_2'}$ over a Boltzmann distribution of the collision energy E,

$$k_{j_1j_2\to j_1'j_2'}(T) = \sqrt{\frac{8}{\pi\mu}} (k_B T)^{-\frac{3}{2}} \int_0^{\infty} \sigma_{j_1j_2\to j_1'j_2'}(E) e^{-\frac{E}{k_B T}} E dE \quad (7)$$

where μ is the reduced mass and k_B is the Boltzmann's constant. The excitation rate coefficients $k_{j_1'j_2'\rightarrow j_1j_2}$ can then be obtained from the relaxation rate coefficients by the usual detailed balance formula,

$$\frac{k_{j_1'j_2'\rightarrow j_1j_2}}{k_{j_1j_2\rightarrow j_1'j_2'}} = \frac{(2j_1+1)(2j_2+1)}{(2j_1'+1)(2j_2'+1)} \exp\left(-\frac{\epsilon_{j_2}-\epsilon_{j_2'}+\epsilon_{j_1}-\epsilon_{j_1'}}{k_BT}\right) \tag{8}$$

where ϵ_{j_1} and ϵ_{j_2} are the rigid rotor energies of the two linear molecules

2.3 Critical density

The critical density is the density of interstellar gas for which the rate of de-excitation by spontaneous emission is equal to the rate of de-excitation by collision. At temperature T, it is defined by (Tielens 2005)

$$n_j(T) = \frac{\sum\limits_{i<j} A_{ji}}{\sum\limits_{i\neq j} k_{ji}(T)} \tag{9}$$

where A_{ji} is the Einstein coefficient for the spontaneous emission induced by the transition from state j to state i and $k_{ji}(T)$ is the rate coefficient for the transition $j \rightarrow i$ induced by collision.

The Einstein coefficient A_{ji} for spontaneous emission is defined by

$$A_{ji} = \frac{8\pi^2\nu_{ji}^3}{3\epsilon_0 c^3\hbar} S_{ji} \tag{10}$$

where ν_{ji} is the transition frequency, ϵ_0 the vacuum permittivity, c the speed of light, and S_{ji} the matrix element of the dipole operator. If we consider the spontaneous transitions between the states of a linear rigid rotor, then only the $\Delta j = -1$ transitions are possible. In that case, the matrix elements of the dipole operator are obtained as

$$S_{j,j-1} = \frac{\mu^2 j}{2j+1} \tag{11}$$

where $\mu = 3.10$ D (Kołos et al. 2008) is the dipole moment of C_3N^- at equilibrium geometry.

2.4 Parameters of the calculations

In the present calculation we neglect the vibration of both H_2 and C_3N^-, thus considering both molecules as rigid rotors whose rotational constants are set to their experimental values $B_1 = 60.853\,\mathrm{cm}^{-1}$ (Herzberg & Howe 1959) and $B_2 = 0.1618\,\mathrm{cm}^{-1}$ (Kołos et al. 2008). As the potential well depth is relatively large and the value of the rotational constant B_2 of C_3N^- is small, a large number of rotational levels of this molecule needs to be included in the rotational basis set used for the dynamics. This basis set includes 31 rotational levels of C_3N^- ($0 \leqslant j_2 \leqslant 30$) and 2 rotational levels of H_2 for both *para*–H_2 ($j_1 = 0, 2$) and *ortho*–H_2 ($j_1 = 1, 3$).

The calculations are performed for a grid of collision energies ranging from 0.1 to 2000 cm^{-1}. For each collision energy, the convergence of the results as a function of the maximum value of the intermolecular coordinate R was checked. Owing to the strength of the long-range potential, a maximum value of 200 a_0 was found to be necessary for the lowest collision energies. Furthermore, a 10^{-4} relative criterion was enforced for the convergence of the state-selected quenching cross section as a function of the maximal value of the total angular momentum quantum number J. Because of the large reduced mass of the system, as much as 157 values of J were required to reach this level of relative convergence of the cross section for the highest energies.

2.5 Computational methodology

The aforementioned convergence requirements make the CC calculation prohibitively expensive, even at very low collision energy. We hence developed an MPI version of the DIDIMAT code using an asynchronous task parallelization scheme. This MPI version of the code distributes N tasks over M processors where each task is associated with a propagation of the wave function for a given collision energy and a given value of J.

In order to further reduce the CPU time while keeping a good accuracy of the state-to-state rate coefficients, we also decided to use the UJS method developed by Zhang & Zhang (1999). As a matter of fact, we showed in our recent study dedicated to the rotational excitation of C_3N^- in collisions with He (Lara-Moreno et al. 2017), that this method offers a very good level of accuracy when compared to the exact calculations. The strategy of this method is to compute the state-to-state transition probabilities for selected values of J and then interpolate the missing probabilities in such a way that the rate coefficient at a given temperature can be calculated as accurately as possible.

$$\int_0^\infty P^J(E)\mathrm{e}^{-\frac{E}{k_BT}}\,dE = \int_0^\infty P^0(E - B_iJ(J+1))\mathrm{e}^{-\frac{E}{k_BT}}\,dE \tag{12}$$

where the shifting constant B_i at a given temperature T and for a given value of $J \in [J_i, J_{i+1}]$ is obtained as

$$B_i(T) = \frac{k_BT}{J_{i+1}(J_{i+1}+1) - J_i(J_i+1)} \ln\left(\frac{Q^{J_i}}{Q^{J_{i+1}}}\right) \tag{13}$$

where $Q^J(T)$ is defined as

$$Q^J(T) = \int_0^\infty P^J(E)\mathrm{e}^{-\frac{E}{k_BT}}\,dE \tag{14}$$

As a result equation (7) can be rewritten as

$$k(T) = \left(\frac{2\pi}{\mu^3k_B^3T^3}\right)^{1/2} Q^0(T) \sum_J (2J+1)\mathrm{e}^{-\frac{B_i(T)J(J+1)}{k_BT}} \tag{15}$$

In the previous equations the indexes j_1, j_1', j_2, j_2' have been removed for simplicity.

In the present case we computed the transition probabilities for the values of $J \in \{0, 5, 10, 15, 20, 25, 30, 40, 60, 80\}$ using the CC method. We then interpolated or extrapolated the missing transition probabilities and summed all contribution from $J = 0$ up to 200. In order to check the accuracy of the method, we also performed exact CC calculations for the collisions involving *para*-H_2 and compared the results with those obtained using the UJS procedure in Figure 2.

As it can be seen in this figure, the agreement between the two kinds of calculation is remarkably good, especially for the high temperatures. The mean relative error is smaller than 3% for the whole temperature range while the largest relative error, $\sim 10\%$, is reached at low temperature, $[10 - 50]$ K. In this range of low temperatures, the magnitude of the rate coefficients are anyway very small and the origin of the error is essentially numerical.

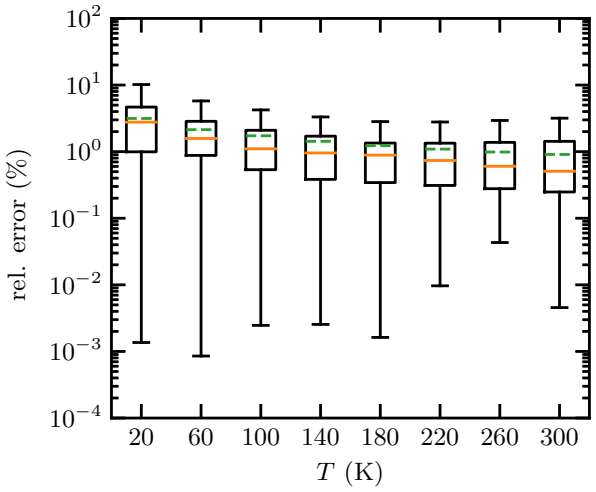

Figure 2. Error in the calculation of *para*–H_2 rates coefficients by using the UJS procedure as a function of temperature. The error populations are depicted by Tukey boxplots. The mean relative error is depicted by dashed green lines.The solid orange line indicates the median (i. e. the second quartile) of the error population, the bottom and top of the box are the first and third quartiles respectively, and the end of the dashed lines are distant from the box by 1.5 times the height of the box.

3 RESULTS

3.1 Rate coefficients

Selected state-to-state rate coefficients for rotational excitation and de-excitation of C_3N^- by collisions with *ortho*- and *para*-H_2 are shown in Table 1 and Figure 3. As can be seen in this figure, the rate coefficients increase slowly as a function of temperature while they monotonously decrease as a fonction of the transferred rotational angular momentum $|\Delta j_2|$. Another important result for this system lies in the striking similarity between *ortho*– and *para*–H_2 rates, especially at high temperatures.

Similarities between *ortho* and *para* rates have also been observed for the collisions of H_2 with anions such as CN^- (Kłos & Lique 2011) and C_6H^- (Walker et al. 2017). These authors suggested that these similarities indicate that the effects from the long-range interaction outweigh those from the short-range interaction. This explanation however does not seem to hold for C_3N^- since the similarities disappear at the lowest temperatures, i.e. when the effects of the long-range potential become more important than those of the short-range potential. Furthermore, the same similarities have been also observed in the collisions of H_2 with HC_3N (Wernli et al. 2007) which involves a long-range potential significantly weaker than in the case of collisions with molecular anions. In this last work, it was shown that the leading term of the short-range potential is common to collisions with *para* and *ortho* conformations while the leading term of the long-range potential contributes only to collisions with the *ortho* conformation. Therefore the resemblance between *ortho* and *para* rates seems to rather result from the features of the short-range interaction, such as angular anisotropy.

Following this line of thought, we analysed the matrix elements of the potential as given by the equation (9) of the seminal paper of Green (1975). These quantities are linear combinations of the radial space-fixed expansion coefficients $A^{\lambda}_{\lambda_1\lambda_2}(R)$ of the potential and are related to their body-fixed counterparts $v^{\mu}_{\lambda_1\lambda_2}(R)$, defined in

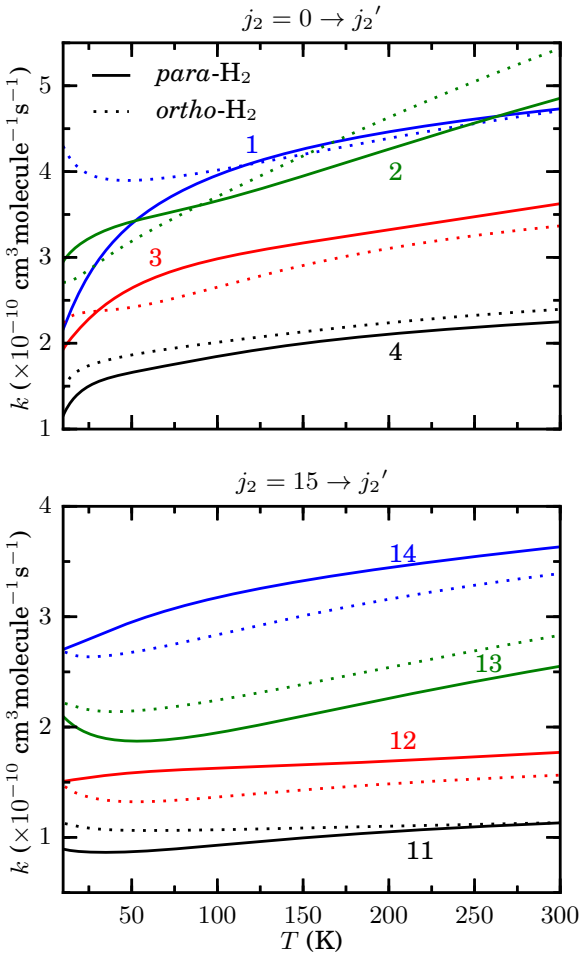

Figure 3. Rotational excitation (upper panel) and de-excitation (lower panel) rate coefficients of C_3N^- in collision with *ortho*– (dotted lines) and and *para*–H_2 (full lines). The curves are labeled by the final state of the transition $j_2 \rightarrow j_2'$

equation (1) of the present paper, by:

$$A^{\lambda}_{\lambda_1\lambda_2}(R) = \left(\frac{2\lambda+1}{16\pi^3}\right)^{-\frac{1}{2}} \sum_{\mu=0}^{\lambda_{\min}} (-1)^{\mu} \langle \lambda_1 \mu \lambda_2 -\mu | \lambda 0 \rangle v^{\mu}_{\lambda_1\lambda_2}(R) \quad (16)$$

For the collisions involving *para*–H_2 ($j_1 = 0$), the coupling matrix elements are non zero only if $\lambda_1 = 0$ while for those of *ortho*–H_2 ($j_1 = 1$) both $\lambda_1 = 0$ and 2 are possible.

As can be seen in Figure 4 where the first six $A^{\lambda}_{\lambda_1\lambda_2}(R)$ coefficients are represented, the short-range interaction appears to be dominated by the attractive A^0_{00} term which gives non zero contributions for collisions involving both *ortho*– and *para*–H_2. This term is isotropic and its minimum has an intermolecular distance R close to those of the minima of the PES. The major contribution to this term is the charge–induced dipole interaction. In contrast, the strongest contribution to the long-range part of the potential is associated with the charge-quadrupole A^2_{20} term which gives non zero potential matrix elements only for the *ortho* states of H_2. This may explain why the difference between *para* and *ortho* rates represented in Figure 3 are larger at low temperatures, while decreasing at higher temperature. This explanation however holds only for the lowest *para* and

Table 1. State to state rate coefficients $k_{j_1,j_2 \to j_1',j_2'}$ ($cm^3 molecule^{-1} s^{-1}$) for the rotational excitation of C_3N^- in collision with *para* ($j_1 = 0$) and *ortho* ($j_1 = 1$) H_2 for various temperature values. Power of 10 is denoted in parenthesis. The complete set of rate coefficient is available in the online supplementary material

j_1	j_2	j_1'	j_2'	T = 10 K	T = 100 K	T = 300 K
0	0	0	1	2.16(−10)	3.95(−10)	4.73(−10)
1	0	1	1	4.28(−10)	3.99(−10)	4.69(−10)
0	0	0	2	2.94(−10)	3.65(−10)	4.85(−10)
1	0	1	2	2.70(−10)	3.68(−10)	5.41(−10)
0	0	0	3	1.92(−10)	2.97(−10)	3.62(−10)
1	0	1	3	2.22(−10)	2.64(−10)	3.35(−10)
0	0	0	4	1.15(−10)	1.84(−10)	2.24(−10)
1	0	1	4	1.46(−10)	2.00(−10)	2.38(−10)
0	5	0	6	2.09(−10)	3.51(−10)	4.20(−10)
1	5	1	6	2.83(−10)	3.32(−10)	3.94(−10)
0	5	0	7	1.33(−10)	2.46(−10)	3.30(−10)
1	5	1	7	1.46(−10)	2.74(−10)	3.57(−10)
0	5	0	8	7.06(−11)	1.97(−10)	2.43(−10)
1	5	1	8	8.13(−11)	1.73(−10)	2.15(−10)
0	5	0	9	3.36(−11)	1.27(−10)	1.73(−10)
1	5	1	9	4.46(−11)	1.49(−10)	1.73(−10)
0	10	0	11	1.69(−10)	3.27(−10)	3.89(−10)
1	10	1	11	1.80(−10)	2.96(−10)	3.65(−10)
0	10	0	12	8.30(−11)	2.07(−10)	2.93(−10)
1	10	1	12	8.78(−11)	2.35(−10)	3.21(−10)
0	10	0	13	3.43(−11)	1.70(−10)	2.11(−10)
1	10	1	13	3.41(−11)	1.45(−10)	1.88(−10)
0	10	0	14	1.17(−11)	9.98(−11)	1.43(−10)
1	10	1	14	1.49(−11)	1.15(−10)	1.43(−10)
0	15	0	16	1.38(−10)	3.13(−10)	3.77(−10)
1	15	1	16	1.32(−10)	2.78(−10)	3.50(−10)
0	15	0	17	5.18(−11)	1.88(−10)	2.73(−10)
1	15	1	17	5.46(−11)	2.17(−10)	3.04(−10)
0	15	0	18	1.81(−11)	1.58(−10)	1.99(−10)
1	15	1	18	1.65(−11)	1.30(−10)	1.73(−10)
0	15	0	19	4.92(−12)	8.85(−11)	1.30(−10)
1	15	1	19	5.97(−12)	1.01(−10)	1.32(−10)
0	20	0	21	1.24(−10)	3.09(−10)	3.72(−10)
1	20	1	21	9.64(−11)	2.69(−10)	3.46(−10)
0	20	0	22	3.08(−11)	1.75(−10)	2.63(−10)
1	20	1	22	3.52(−11)	2.02(−10)	2.95(−10)
0	20	0	23	9.52(−12)	1.45(−10)	1.90(−10)
1	20	1	23	7.59(−12)	1.20(−10)	1.69(−10)
0	20	0	24	2.09(−12)	8.16(−11)	1.27(−10)
1	20	1	24	2.43(−12)	9.34(−11)	1.32(−10)

ortho states of H_2 and another explanation would need to be found if further calculations show that the similarities are also observed for the higher rotational states of *ortho*–H_2 ($j_1 = 3, 5 \ldots$) and *para*–H_2 ($j_1 = 2, 4 \ldots$).

We now turn our attention to the comparison of the rotational transition rate coefficients of the anions CN^-, C_3N^-, and C_6H^- in collision with H_2. The PES of these three collisional systems are not much different. In all three PES, the global minimum is a colinear structure and the dissociation energies are in the range 700–900 cm^{-1}. For H_2–CN^- and H_2–C_3N^-, the secondary minimum is also a colinear structure, while it is a T-shape structure for H_2–C_6H^-. Moreover, the A^0_{00}, A^2_{20}, and A^2_{02} expansion coefficients are the leading terms for all three PES, as shown in Figures 4, S1 and S2 (see supplementary material). Figure 5 shows the rate coefficients at 100 K for the de-excitation transitions from the initial rotational state $j_2 = 10$ of the three anions through collision with *para*–H_2.

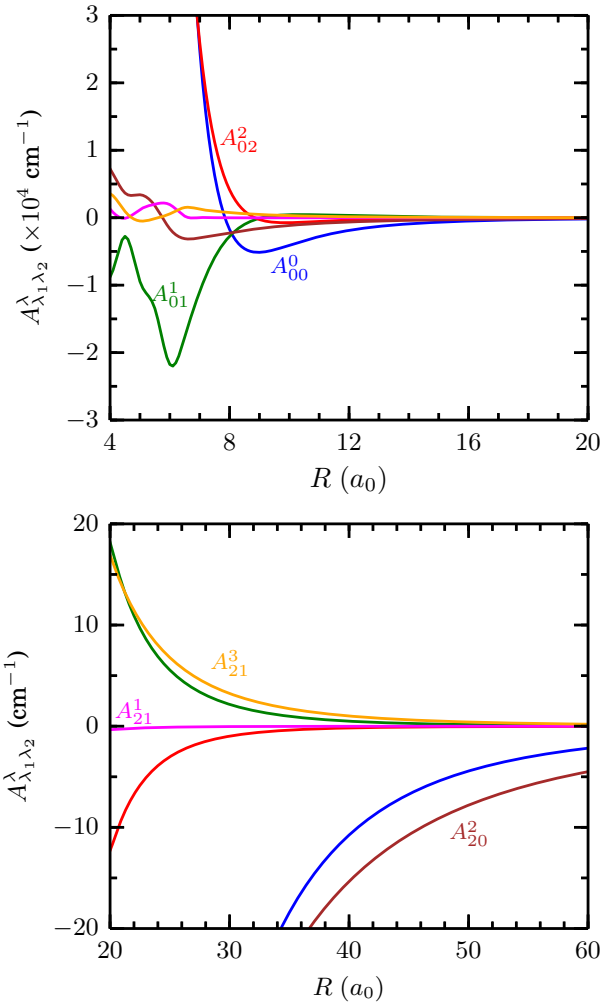

Figure 4. First six expansion coefficients $A^\lambda_{\lambda_1\lambda_2}$ as a function of the intermolecular distance. The curves are labeled by their corresponding indexes.

Figure 6 shows the same comparison, but only for C_6H^- and C_3N^-, at 100 K and from the initial state $j_2 = 20$. Very similar figures can be obtained for the de-excitation rate coefficients in the whole common range of temperature for which data are available, namely 10–100 K, and for both *para*– and *ortho*–H_2.

As can be seen on these figures, the rate coefficients for C_6H^- are in remarkably good agreement with those for C_3N^- for $|\Delta j_2| \lesssim 10$, and for larger values of $|\Delta j_2|$, the rate coefficients for C_3N^- becomes progressively smaller than the one for C_6H^-. The agreement between the rate coefficients for CN^- and those of C_3N^- and C_6H^- is also relatively good for the transitions with $|\Delta j_2| \lesssim 5$ while for larger values of $|\Delta j_2|$, the CN^- rates become much smaller than the other ones. A simple explanation involving the size of the molecules can be proposed. The three anions are linear molecules, but they are of significantly different lengths. A longer molecule imply a stronger anisotropy of the short-range interaction potential and also a smaller rotational constant. Both features are expected to enhance the transitions with large transferred rotational angular momentum, as observed in Figures 5 and 6.

The most interesting result is nevertheless the remarkably good agreement between the rate coefficients for the lowest values of $|\Delta j_2|$. This suggest that collisional rates of H_2 with the larger chains

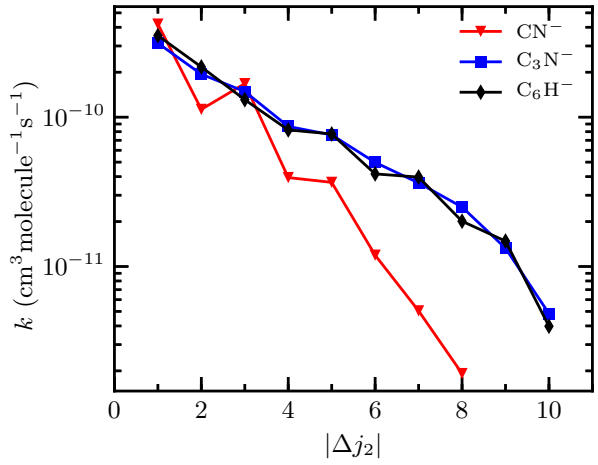

Figure 5. De-excitation rate coefficients of CN^-, C_3N^-, and C_6H^- in initial state $j_2 = 10$ by collision with *para*–H_2 at 100 K as a function of the magnitude of the transferred angular momentum $|\Delta j_2|$

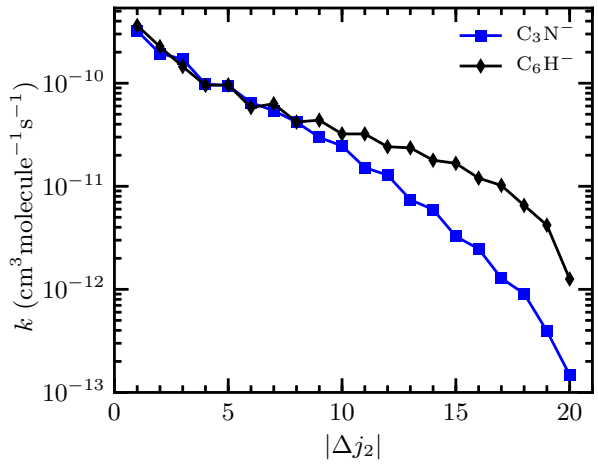

Figure 6. De-excitation rate coefficients of C_3N^- and C_6H^- in initial state $j_2 = 20$ by collision with *para*–H_2 at 100 K as a function of the magnitude of the transferred angular momentum $|\Delta j_2|$

of the two $C_{2n+1}N^-$ and $C_{2n}H^-$ families could be extrapolated from those now available for C_3N^- and C_6H^-. One reason for such a good agreement might be the nature of the long-range interaction. For anion–H_2 collisional systems, the leading long-range interactions are the charge-quadrupole interaction, which scales as R^{-3}, and the charge-induced dipole which scales as R^{-4}. These interactions are independent of the nature of the ionic monomer. Cations–H_2 collisional systems are also expected to show the same behavior.

We conclude this study by checking the validity of the He/*para*–H_2 scaling law for the rotational transitions of C_3N^-. In this approximation, the inelastic collisional rates of any molecule with *para*–H_2 ($j_1 = 0$) are derived from those with He by using the following reduced mass ratio:

$$r = \frac{k_{0,j\to 0,j'}(H_2)}{k_{j\to j'}(He)} = \sqrt{\frac{\mu_{He-X}}{\mu_{H_2-X}}} \approx \sqrt{2} \qquad (17)$$

where μ_{A-B} stands for the reduced mass of the A+B collisional system. For C_3N^-, the ratio between the previously calculated rates for the collisions with He (Lara-Moreno et al. 2017) and those calculated in the present work for *para*–H_2 is in average equal to 3 and can reach values as large as 6 at low temperature. The averaged value is then more than twice larger than the expected value of $r \approx 1.41$, thus leading to a relatively large average error (< 50%) for the scaled *para*–H_2 rate coefficients. In addition, we found that the use of the He/*para*–H_2 scaling law would introduce a spurious propensity rule $|\Delta j_2| = 2$ which is not observed in the accurately computed rate coefficients with *para*–H_2.

In order to better understand the origin of the failure of the He/*para*–H_2 scaling law for this system, we compare the H_2–C_3N^- PES averaged over the rotational ground state of *para*–H_2 with the He–C_3N^- PES in Figure 7. Let us note that the averaging washes out the global and secondary potential wells seen in Figure 1 since the rotation of H_2 involves to pass through a large energy barrier located around $\theta_1 = 90°$ (Lara-Moreno et al. 2019). We see at first that the long-range potential is stronger in the case of *para*–H_2. This is mainly due to the large difference between the isotropic polarizabilities[1] of He ($\alpha_{He} = 1.38\ {a_0}^3$) and H_2 ($\alpha_{H_2} = 5.4\ {a_0}^3$) since the charge–induced dipole interaction, proportional to $-\frac{\alpha}{R^4}$, is the leading contribution to both interaction potentials at large distance. As a result, the magnitude of the long-range potential of C_3N^- with H_2 is almost five times larger than its He counterpart. This may explain the quite large value $r \approx 6$ found at low collision energy. A second difference is related with the potential wells which are both associated with a distorted T-shape geometry, but the *para*–H_2–C_3N^- well is slightly deeper than the He–C_3N^- one by a few cm^{-1}. A third difference stems from the symmetry of the two PES with respect to the inversion of the C_3N^- molecule. Both PES are not symmetric, but the He–C_3N^- PES is slightly more symmetrical than the *para*–H_2–C_3N^- one if we compare the -10 cm^{-1} contour lines. This last point may explain the differences observed in the propensity rules.

3.2 Critical densities

The local thermodynamic equilibrium (LTE) is established if the population of excited levels is given by the Boltzmann's law. This occurs only if the rate of spontaneous emission is significantly smaller than the rate of de-excitation by collision and therefore only if the density of gas is significantly larger than the critical density.

C_3N^- has been detected in the circumstellar envelope (CSE) of the carbon star IRC +10216 and in the Taurus molecular cloud 1 (TMC-1). In a CSE, the gas density and temperature are decreasing functions of the radius r. The shell in which the largest abundance of C_3N^- is predicted by chemical models is approximately defined by the radius range 10^{16}–10^{18} cm (Cernicharo et al. 2008; Millar 2016). In this shell, the gas density is assumed to fall as r^{-2} from more than 10^5 cm^{-3} to less than 10^2 cm^{-3} while temperature is assumed to decrease from 40 to 10 K (Cordiner & Millar 2009). In the dark cloud TMC-1, the gas density is believed to be about 10^4 cm^{-3} with temperature in the range 10–30 K.

Figure 8 shows that the critical densities for the lowest rotational levels ($j \lesssim 5$) are relatively small and are reached in most of the interstellar environments where C_3N^- has been detected. For the higher rotational levels, the LTE cannot be taken for granted. It

[1] Calculated using finite field method at CCSD(T)/aug-cc-pVQZ level

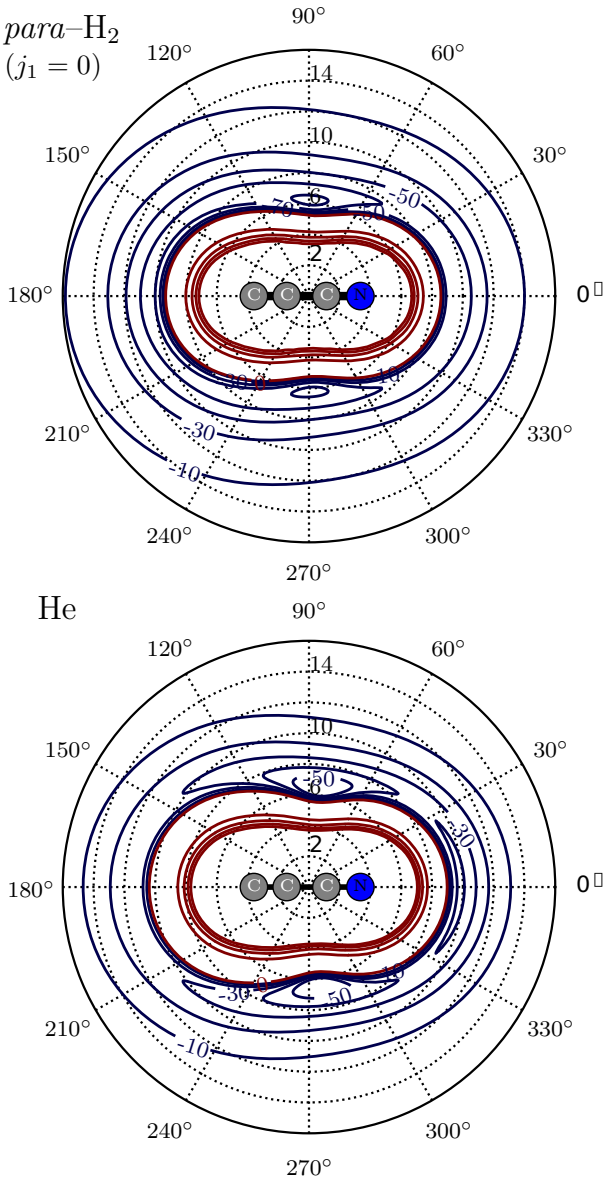

Figure 7. 2D polar contour plots of the interaction of C_3N^- with *para* H_2(upper panel) and He (lower panel). The interaction of C_3N^- with H_2 is represented by a potential averaged over the rotational wave function $|j_1 = 0, m_1 = 0\rangle$. Contour levels are equally spaced and labeled by the energy in cm^{-1}. The contours are blue for negative interaction energy, and red for positive one. The origin of coordinates corresponds to the centre of mass of C_3N^-.

is clearly dependent of the temperature and gas density. Sufficiently hot (kinetic temperature $T \gtrsim 40$ K) and diffuse ($n \lesssim 10^4$ cm^{-3}) conditions will not allow LTE.

4 CONCLUSIONS

State-to-state rotational excitation and de-excitation rate coefficients of C_3N^- in collisions with *ortho*– and *para*–H_2 in the temperature range [10, 300] K were obtained by combining CC calculations and the UJS procedure. We find that the relative error offered by the UJS method is always less than 10% demonstrating once again that the UJS procedure is a very good approximation which reduces computational cost without losing much accuracy. On the other hand, we found once again that the application of the He/*para*–H_2 scaling law to the He–C_3N^- rate coefficients would lead to relatively large error(< 50%) for the *para*–H_2 rates.

The strongly repulsive nature of the H_2-C_3N^- interaction at short range leads to close similarities between *ortho* and *para* rates and enhances transition associated with large transferred angular momentum. The rotational transition rates of C_3N^- in collision with *para*–H_2 are quite close to those with *para*–H_2. The same effect was previously observed for CN^- and C_6H^-.

The rotational de-excitation rate coefficients of the three anions CN^-, C_6N^- and C_3N^- are in close agreement for small values of the transferred rotational angular momentum $|\Delta j_2|$, and a remarkably good agreement is observed between C_6N^- and C_3N^- for $|\Delta j_2| \lesssim 10$. This agreement arises probably from the fact that the leading long-range interactions, namely the charge-quadrupole and the charge-induced dipole interactions, are independent of the charged species. This opens the way for a quantitative extrapolation of the rotational transition rate coefficients of anions in collision with H_2, such as for example, the carbon chains of the two $C_{2n+1}N^-$ and $C_{2n}H^-$ families which have been discovered in the ISM.

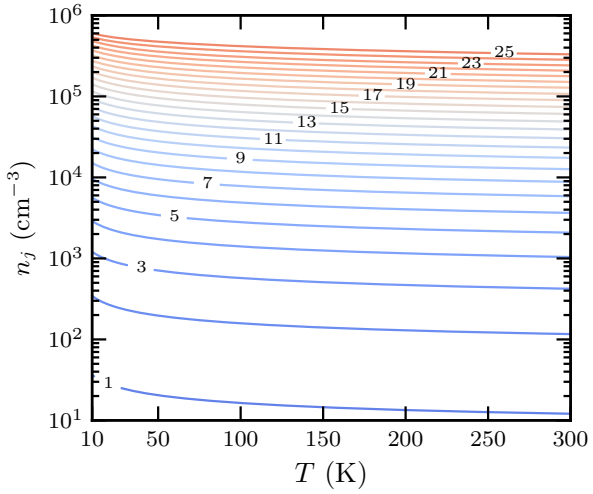

Figure 8. Critical densities for the rotational levels of C_3N^-. The curves are labeled by the rotational quantum number.

ACKNOWLEDGEMENTS

This research has been supported by the *Agence Nationale de la Recherche* (Project ANR-AnionCosChem). Computer time for this study was provided by the *Mésocentre de Calcul Intensif Aquitain* which is the computing facilities of *Université de Bordeaux et Université de Pau*.

REFERENCES

Agúndez M., et al., 2010, A&A, 517, L2
Boys S., Bernardi F., 1970, Mol. Phys., 19, 553

Brünken S., Gupta H., Gottlieb C. A., McCarthy M. C., Thaddeus P., 2007, ApJ, 664, L43
Cernicharo J., Guélin M., Agúndez M., Kawaguchi K., McCarthy M., Thaddeus P., 2007, A&A, 467, L37
Cernicharo J., Guélin M., Agúndez M., McCarthy M. C., Thaddeus P., 2008, ApJ, 688, L83
Chefdeville S., Stoecklin T., Naulin C., Jankowski P., Szalewicz K., Faure A., Costes M., Bergeat A., 2015, ApJ, 799, L9
Cordiner M. A., Millar T. J., 2009, ApJ, 697, 68
Dalgarno A., McCray R. A., 1973, ApJ, 181, 95
Denis-Alpizar O., Stoecklin T., Halvick P., Dubernet M.-L., 2013, J. Chem. Phys., 139, 204304
Denis-Alpizar O., Stoecklin T., Guilloteau S., Dutrey A., 2018, MNRAS, 478, 1811
Green S., 1975, J. Chem. Phys., 62, 2271
Guillon G., Stoecklin T., 2012, MNRAS, 420, 579
Guillon G., Stoecklin T., Voronin A., Halvick P., 2008, J. Chem. Phys., 129, 104308
Herbst E., 1981, Nature, 289, 656
Herzberg G., Howe L. L., 1959, Can. J. Phys., 37, 636
Kendall R. A., Dunning T. H., Harrison R. J., 1992, J. Chem. Phys., 96, 6796
Kłos J., Lique F., 2011, MNRAS, 418, 271
Kołos R., Gronowski M., Botschwina P., 2008, J. Chem. Phys., 128
Lara-Moreno M., Stoecklin T., Halvick P., 2017, MNRAS, 467, 4174
Lara-Moreno M., Stoecklin T., Halvick P., 2019, Phys. Chem. Chem. Phys.
Lique F., Toboła R., Kłos J., Feautrier N., Spielfiedel A., Vincent L. F. M., ński G. C., Alexander M. H., 2008, A&A, 478, 567
Manolopoulos D. E., 1986, J. Chem. Phys., 85, 6425
McCarthy M. C., Gottlieb C. A., Gupta H., Thaddeus P., 2006, ApJ, 652, L141
Millar T. J., 2016, J. Phys.: Conf. Ser., 728, 052001
Sarre P., 1980, J. Chim. Phys., 77, 769
Thaddeus P., Gottlieb C. A., Gupta H., Brünken S., McCarthy M. C., Agúndez M., Guélin M., Cernicharo J., 2008, ApJ, 677, 1132
Tielens A. G. G. M., 2005, The Physics and Chemistry of the Interstellar Medium. Cambridge University Press
Walker K. M., Yang B. H., Stancil P. C., Balakrishnan N., Forrey R. C., 2014, ApJ, 790, 96
Walker K. M., Lique F., Dumouchel F., Dawes R., 2017, MNRAS, 466, 831
Werner H.-J., et al., 2012, MOLPRO, version 2012.1, a package of ab initio programs
Wernli M., Wiesenfeld L., Faure A., Valiron P., 2007, A&A, 464, 1147
Zhang D. H., Zhang J. Z. H., 1999, J. Chem. Phys., 110, 7622

This paper has been typeset from a TEX/LATEX file prepared by the author.